Evaporation of Droplets on Superhydrophobic Surfaces: Surface Roughness and Small Droplet Size Effects

Xuemei Chen,[1] Ruiyuan Ma,[2] Jintao Li,[1] Chonglei Hao,[1] Wei Guo,[1] B. L. Luk,[1] Shuai Cheng Li,[3] Shuhuai Yao,[2] and Zuankai Wang[1,*]

[1]*Department of Mechanical and Biomedical Engineering, City University of Hong Kong, Hong Kong 999077, China*
[2]*Department of Mechanical Engineering, The Hong Kong University of Science and Technology, Hong Kong 999077, China*
[3]*Department of Computer Science, City University of Hong Kong, Hong Kong 999077, China*

(Received 10 January 2012; revised manuscript received 20 July 2012; published 10 September 2012; publisher error corrected 12 September 2012)

Evaporation of a sessile droplet is a complex, nonequilibrium phenomenon. Although evaporating droplets upon superhydrophobic surfaces have been known to exhibit distinctive evaporation modes such as a constant contact line (CCL), a constant contact angle (CCA), or both, our fundamental understanding of the effects of surface roughness on the wetting transition remains elusive. We show that the onset time for the CCL-CCA transition and the critical base size at the Cassie-Wenzel transition exhibit remarkable dependence on the surface roughness. Through global interfacial energy analysis we reveal that, when the size of the evaporating droplet becomes comparable to the surface roughness, the line tension at the triple line becomes important in the prediction of the critical base size. Last, we show that both the CCL evaporation mode and the Cassie-Wenzel transition can be effectively inhibited by engineering a surface with hierarchical roughness.

DOI: 10.1103/PhysRevLett.109.116101 PACS numbers: 68.08.Bc, 68.03.Fg

Understanding and controlling the droplet contact line dynamics on textured surfaces, especially superhydrophobic surfaces, is of critical importance for a wide range of applications including self-cleaning, drag reduction, water harvest, anticorrosion, thermal management, and biosensing [1–11]. Although the contact line dynamics of a droplet on hydrophobic or superhydrophobic surfaces in the equilibrium condition has been extensively studied [12–15], the contact line dynamics during the phase change processes such as evaporation and condensation remains relatively less exploited. In the case of droplet evaporation, most studies to date focus either on the investigation of the evaporation patterns [16–18] or on the evaporation modes including a constant contact line (CCL), a constant contact angle (CCA), and a mixed mode on various surfaces or on the Cassie-Wenzel transition occurring at the late stage of evaporation [19–21]. Despite extensive progress, our fundamental understanding of how the surface roughness affects the wetting transition remains elusive. In this work, we systematically investigated the full spectrum of evaporation dynamics of droplets on rough surfaces based on microscopic and macroscopic observations and found that the wetting transition exhibited remarkable dependence on the geometric arrangement of the substrate. In particular, when the droplet shrinks to a size that is comparable to the substrate roughness, the line tension becomes more important. We developed general models to accurately predict the CCL-CCA transition onset time and critical base size at the Cassie-Wenzel transition, respectively.

We first studied the evaporation dynamics on the microtextured silicon surfaces with pillar-to-pillar spacings (L) of 10, 20, and 40 μm, respectively. For simplicity, these surfaces are denoted as m10, m20, and m40, respectively. The diameter (D) and height (H) of pillars of all three surfaces are set as 20 and 80 μm, respectively. All these surfaces were fabricated by using standard microfabrication processes including photolithography and deep reactive-ion etching [22,23]. To render them superhydrophobic, the samples were treated with ~1 mM hexane solution of perfluorooctyl trichlorosilane for ~30 min, followed by heat treatment at ~150 °C in air for 1 h. Figure 1(a) shows the scanning electron microscopy image of the as-fabricated m40 surface. The evaporation process was carried out at ~17 °C, and the relative humidity was ~65%. The water droplets on the microstructured surface (m10, m20, and m40) exhibited three distinctive evaporation stages: a CCL mode with a decreasing contact angle at the early stage, a CCA mode with a shrinking contact line, and a mixed mode with a Cassie-Wenzel transition. The evaporating droplet in the CCL and CCA modes stayed in a Cassie state, as can be clearly seen from Fig. 1(b). Although all the microstructured surfaces exhibit three evaporation stages, we found that the CCL-CCA transition exhibited remarkable sensitivity to the geometry arrangement: The CCL-CCA transition onset time on m40 surface is the lowest (2558 s), which is ~26% lower than the m10 surface (3230 s) [see Figs. 1(c) and 1(d)].

The existence of a CCL stage on the microtextured surface might be explained by considering the local forces at the triple contact line [10,24]. The depinning force F_D can be expressed as $2R_b\sigma_{lg}(\cos\theta - \cos\theta_c)$, where R_b is the base radius of droplet, σ_{lg} is the surface tension of water, θ is the dynamic contact angle during the evaporation, and θ_c is the apparent contact angle on the

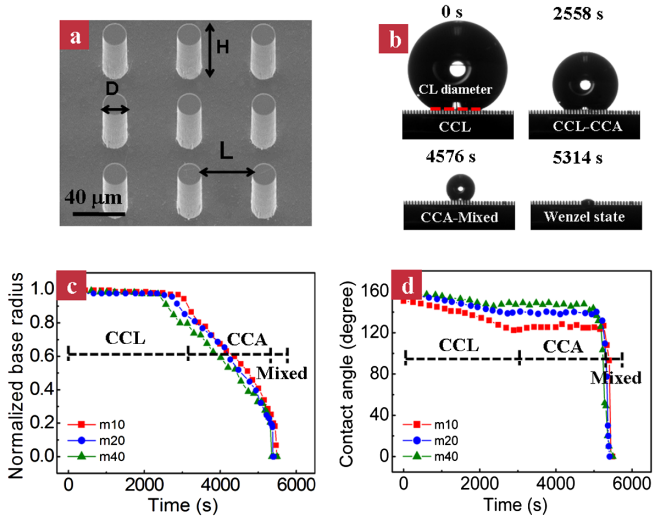

FIG. 1 (color online). (a) Scanning electron microscopy image of a microstructured surface with pillar-to-pillar spacing $L = 40\ \mu$m (m40). (b) Time-dependent images of an evaporating droplet on the m40 surface. (c),(d) Time evolutions of normalized contact base radius and contact angle on microstructured surfaces (m10, m20, and m40).

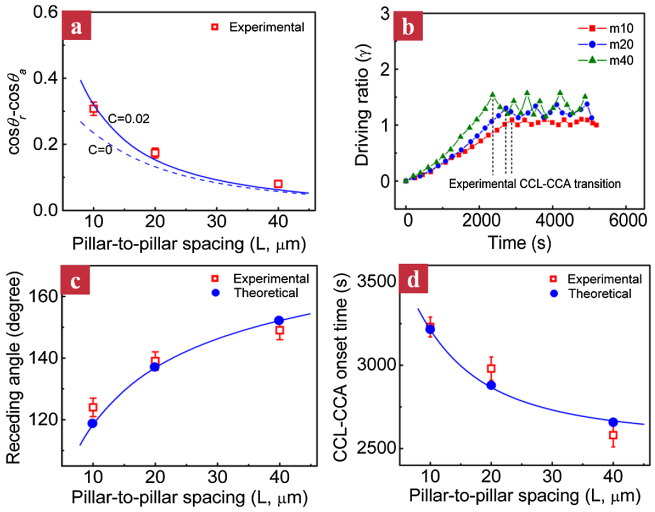

FIG. 2 (color online). (a) Contact angle hysteresis ($\cos\theta_r - \cos\theta_a$) as a function of pillar-to-pillar spacing (L). The theoretical predictions are obtained through the equation $\cos\theta_r - \cos\theta_a = \varnothing(\cos\theta_{ro} - \cos\theta_{ao}) + cD^2/L^2$, where c is a constant. When $c = 0$, the theoretical value is underestimated, whereas when c is equal to 0.02, there is a good fit between our experimental (squares) and theoretical data (solid line). (b) Time evolutions of the driving ratio (γ) on microtextured surfaces (m10, m20, and m40). γ is less than 1.0 in the CCL stage and fluctuates around 1 after transiting to the CCA mode. (c) The effect of pillar-to-pillar spacing (L) on the critical receding angle based on theoretical analysis (solid line) and experimental measurements (square). The theoretical receding angles are obtained when the driving ratio $\gamma = 1$. (d) The effect of pillar-to-pillar spacing (L) on the onset time corresponding to the CCL-CCA transition based on both experimental (squares) and theoretical prediction (solid line).

rough surface. The pinning force F_P can be expressed as $2R_b\sigma_{lg}[(\cos\theta_{ro} - \cos\theta_{ao})\varnothing + H_r]$, where θ_{ro} and θ_{ao} are receding and advancing contact angles on the flat surface ($\sim 80°$ and $120°$ in our case), respectively, and $\varnothing$ is the solid fraction. H_r denotes the adhesive force due to surface roughness and heterogeneity ($H_r \sim cD^2/L^2$) [1]. The constant c is obtained by fitting the measured contact angle hysteresis with the theoretical data. In our case, $c = 0.02$ [see Fig. 2(a)]. Assuming the ratio of depinning force to the pinning force as the driving ratio (γ), we have

$$\gamma = F_D/F_P = (\cos\theta - \cos\theta_c)/[(\cos\theta_{ro} - \cos\theta_{ao})\varnothing + H_r]. \quad (1)$$

Thus, based on the dynamic contact angle obtained in the experiments, the progression of driving ratio (γ) with time is plotted in Fig. 2(b). We can see that, at the beginning of evaporation, γ is less than 1, indicating that the droplet stays in the sticky CCL mode. When γ reaches the maximum (~ 1.1, 1.3, and 1.5 for three surfaces, respectively), the droplet transits to CCA mode.

To theoretically predict the CCL-CCA transition onset time, we referred to the spherical cap model derived by Rowan *et al.*, which describes the evaporation time (t) of a droplet in the CCL stage [25,26]. Briefly, t is governed by the following equations:

$$t = \frac{R_{b0}^2}{2\xi}[F(\theta_{cri}) - F(\theta_0)], \quad F(\theta) = \ln\left[\tan\left(\frac{\theta}{2}\right)\right] + \frac{1}{1+\cos\theta},$$
$$\xi = \frac{2D_f(c_\infty - c_0)}{\rho}, \quad (2)$$

where θ_{cri} is the critical receding angle, θ_0 is the apparent contact angle, R_{bo} is the initial base radius of the droplet, D_f is the diffusion coefficient of water (1.83×10^{-5} m^2/s), C_∞ and C_o are the concentration of saturated water vapor at infinity (9.425 g/m^3) and immediately surrounding the droplet (14.5 g/m^3) [27], respectively, and ρ is the liquid density (1 g/cm^3). By assuming γ equivalent to 1.0 in Eq. (1), the critical receding angle on m10, m20, and m40 surfaces at the CCL-CCA transition are calculated to be 119°, 137°, and 152°, respectively, which are in good agreement with our experimental data on the transition points [Fig. 2(c)]. As shown in Fig. 2(d), the time prediction obtained from our model is in reasonable agreement with our experimental observation: The larger the spacing, the more favorable for CCL-CCA transition.

The surface that is more prone to CCL-CCA transition also corresponds to a larger critical base size at the Cassie-Wenzel transition. The critical drop base radius R_b^* on the m40 surface at the Cassie-Wenzel transition is $\sim 130\ \mu$m, which is much larger than those on m10 ($\sim 80\ \mu$m) and m20 ($\sim 100\ \mu$m) surfaces [Fig. 3(c)]. In order to elucidate the effect of surface roughness on the Cassie-Wenzel

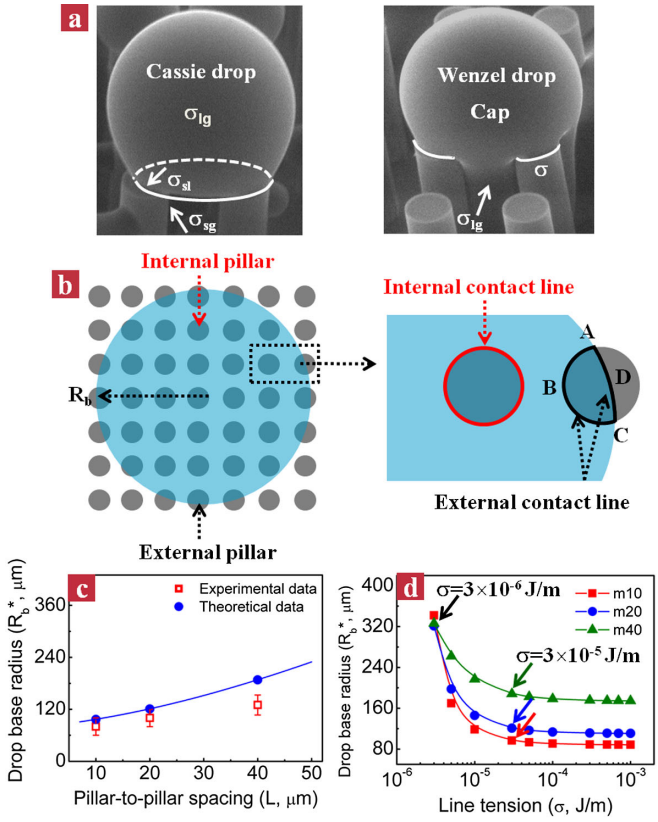

FIG. 3 (color online). (a) Environmental scanning electron microscope images of a Cassie- and Wenzel-state droplet with surface tension and line tension labeled. (b) Schematic drawing of a Cassie drop sitting on the microstructured surface. The enlarged image shows the contact line of single internal and external pillars. (c) Comparison of the critical drop base radius R_b^* at the Cassie-Wenzel transition on various surfaces between experimental data (square) and theoretical prediction using the global interfacial energy analysis (solid line). (d) The variation of the critical drop base radius R_b^* under different line tension values. When the line tension is larger than 3×10^{-5} J/m, the theoretical R_b^* remains almost unchanged, whereas below this critical line tension value, there is a sharp increase in R_b^* value, corresponding to a large discrepancy between theoretical and experimental data.

transition, we first considered a number of models including the touchdown model, pinning instability model, etc. [28–31]. However, these models could not accurately predict the accurate droplet base radius, partially due to the fact that the droplet size at the late stage of evaporation is very comparable to our substrate roughness. For example, in the touchdown model [28], the critical radius R^* ($R^* = R_b^*/\sin\theta$) of the droplet on the m40 surface at the Cassie-Wenzel transition is $\sim L^2/H = 20$ μm, which is much smaller than the observed droplet base radius R_b^* (~ 130 μm).

To enable a more accurate prediction of the critical base size, we compared the interfacial energy of a droplet at both Cassie and Wenzel states [32–34]. Note that at the late stage of evaporation previous to the Cassie-Wenzel transition, the droplet size is comparable to the pillar diameter. Under this condition, the line tension (σ), the excess of free energy per unit length of the three-phase contact line, is not negligible in the energy analysis because of the increasing line-to-surface and line-to-volume ratios in the small droplet [35–40] [Fig. 3(a)]. Thus, the total energy in the system includes the interfacial energy associated with the solid-gas (σ_{sg}), liquid-gas (σ_{lg}), and solid-liquid (σ_{sl}) as well as the line energy. Moreover, since the pillars underneath the evaporating droplet exhibit different contact lines and the total number of pillars is limited, it is important to separate the inside pillars, which are completely covered by the droplet, from external ones, which are partially covered by the droplet, in the calculation of the interfacial energy of the system. Thus, we first calculated the number of internal pillars (N_1) as well as external pillars (N_2). Based on the study of the Gaussian circle problem and the parameter settings of the linear regression method [41–44], we obtained $N_1 = \frac{\pi R_b^2}{(L+D)^2}$ and $N_2 = \frac{1.738\pi R_b D}{(L+D)^2}$ (see Supplemental Material [45]). Accordingly, to calculate the total interfacial energy, the solid-liquid surface area (A_{sl}), the solid-gas surface area (A_{sg}), and the total contact line (L_T) were divided into two parts, respectively. Briefly, A_{sl} consists of the liquid surface area contacting with the external pillars ($A_{sl\text{-}ex}$) and the inside pillars ($A_{sl\text{-}in}$), A_{sg} consists of the gas surface area contacting with the external pillars ($A_{sg\text{-}ex}$) and the inside pillars ($A_{sg\text{-}in}$), and L_T includes the contact line contributed by the external pillars (L_{ex}) and the inside pillars (L_{in}) [see Fig. 3(b)].

Thus, the energy associated with the Cassie state E_C can be expressed as

$$E_C = A_{cap}\sigma_{lg} + A_{lg}\sigma_{lg} + (A_{sl\text{-}in} + A_{sl\text{-}ex})\sigma_{sl} + (A_{sg\text{-}in} + A_{sg\text{-}ex})\sigma_{sg} + (L_{in} + L_{ex})\sigma, \quad (3)$$

where A_{cap} is the surface area of the water cap in contact with the gas, which can be expressed as $\frac{2\pi R_b^2}{1+cos\theta_{cri}}$ and A_{lg} is the base liquid area contacting with the gas and is equivalent to $\pi R_b^2 - A_{sl\text{-}in} - A_{sl\text{-}ex}$, where $A_{sl\text{-}in} = N_1\frac{\pi D^2}{4}$ and $A_{sl\text{-}ex} = 0.119N_2\pi D^2$. $A_{sg\text{-}in} = N_1\pi DH + \pi R_b^2 - A_{sl\text{-}in} - A_{sl\text{-}ex}$ and $A_{sg\text{-}ex} = N_2 L_{ABC} H = 0.546N_2\pi DH$. $L_{in} = N_1\pi D$ and $L_{ex} = N_2(L_{ABC} + L_{ADC}) = 0.834N_2\pi D$ (see Supplemental Material [45]), where $N_2 L_{ABC}$ and $N_2 L_{ADC}$ are the total inside and outside arc length of water contact with the external pillars, respectively.

Similarly, the energy in the Wenzel state is governed by

$$E_W = A_{cap1}\sigma_{lg} + (2\pi R_b - N_2 L_{ADC})H\sigma_{lg} + [\pi R_b^2 + N_1\pi DH + N_2 L_{ABC} H]\sigma_{sl} + (2\pi R_b + 2N_2 H)\sigma, \quad (4)$$

where A_{cap1} is the surface area of the water cap in contact with the gas, which can be expressed as $\frac{2\pi R_b^2}{1+\cos\theta_1}$ and θ_1 is the contact angle of the cap after droplet transiting to the

Wenzel state. Assuming $E_C = E_W$, and R_b and droplet volume remain unchanged during the transient transition, we can get the critical droplet base radius R_b^*. In our calculation, σ is set to be 3×10^{-5} J/m, and this value falls within the wide range (10^{-12}–10^{-4} J/m) found in the literature [36–38]. Figure 3(c) shows both the experimental critical base radius R_b^* and theoretical values obtained from the model for surfaces of different pillar-to-pillar spacing (L). We can see a reasonable agreement between the theoretical and experimental results for m10 and m20 surfaces. Note that the theoretical R_b^* of the m40 surface is ~188 μm, which is relatively larger than our experimental data. In order to illustrate the influence of line tension on the critical droplet base radius R_b^* at the Cassie-Wenzel transition, we compared data under different line tension values (from the order of 10^{-6} to 10^{-3} J/m). As shown in Fig. 3(d), the theoretical R_b^* keeps almost unchanged when the line tension is larger than 3×10^{-5} J/m, while the R_b^* increases sharply when σ is smaller than 3×10^{-5} J/m. For example, when line tension is 3×10^{-6} J/m, R_b^* of the m40 surface is ~326 μm, which is 150% and 73% larger than our experimental data and the theoretical R_b^* in the case of $\sigma = 3 \times 10^{-5}$ J/m, respectively, indicating the significance of line tension in the energy analysis. Note that, among the three surfaces, the m10 surface has the largest line energy percentage (~ 83.8% for the Cassie state and ~78.1% for the Wenzel state) due to its largest pillar density or the smallest pillar-to-pillar spacing (L).

The contact line pinning at the early stage of evaporation and Cassie-Wenzel transition as well as the small droplet size effect at microstructured surfaces could be suppressed by engineering hierarchical surfaces. In order to verify this hypothesis, we deposited uniform nanopillar arrays on the top and valley of our microstructured surfaces (m10, m20, and m40). The nanopillars are ~400 nm in diameter, ~5 μm in height, and ~200–400 nm in pitch. Accordingly, we term three hierarchical surfaces as mn10, mn20, and mn40. Figure 4(a) shows the snapshots of an evaporating droplet on the mn40 surface over time. Distinct from that on microstructured surfaces, the evaporating droplets on hierarchical surfaces exhibit only two distinct stages: the CCA mode and the mixed mode [see Figs. 4(a)–4(c)]. The disappearance of the sticky CCL mode is ascribed to the large depinning force enabled by the presence of nanoscale roughness. The force analysis at the triple contact line indicates that the depinning force at the micro- or nanopatterned surface is more than 2–5 times larger than the pinning force even at the very beginning of evaporation. As a result of such enhanced dynamic wetting properties, the hierarchical surfaces exhibit superior global depinning at the macroscopic level during the evaporation of droplets in the air; i.e., the sticky CCL evaporation mode is inhibited. Similarly, the presence of nanoscale roughness on the microscale roughness significantly lowers the solid surface energy, and

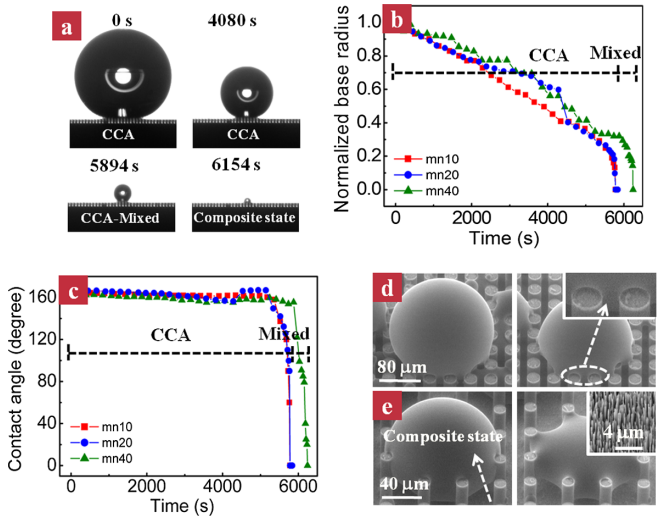

FIG. 4 (color online). (a) Time-dependent images of an evaporating droplet on the mn40 surface. (b),(c) Time evolutions of normalized contact base radius and contact angle on hierarchical surfaces (mn10, mn20, and mn40). Droplet evaporation on all the surfaces exhibits two evaporation modes: a CCA mode and a mixed mode. (d) Snapshots of microdroplet evaporation on the mn10 surface. During the evaporation, the droplet preferentially wets the micropillars rather than the nanopillars, as shown in the inset. (e) Snapshots of microdroplet evaporation on the mn40 surface. The presence of nanoscale roughness in the cavities and at the tops of micropillars (inset) prevents the Cassie-Wenzel transition during the evaporation.

therefore the Cassie-Wenzel transition is prevented [46]. For example, assuming a droplet with a base radius of 130 μm, a size that a droplet will transit to the Wenzel state upon the m40 surface, the Cassie energy on the hierarchical mn40 surface is ~9.5×10^{-7} J, which is much lower than the Wenzel energy calculated for the Wenzel state (~ 1.0×10^{-6} J), indicating that the droplet might stay in a metastable Cassie state. Note that, although we did observe an obvious contact angle change at the late stage of evaporation, the drop remained in a composite state. In order to accurately monitor the wetting state transition with high spatial resolution, we investigated the evaporation dynamics of microdroplets on hierarchical surfaces using an environmental scanning electron microscope (Philips XL-30). We used condensation to produce droplets whose sizes were ~100 μm. We found that, during the evaporation, the droplet preferentially wetted the micropillars instead of nanoscale pillars [see the dashed circles in Fig. 4(d)], suggesting the effect of nanoscale roughness in preventing contact line pinning. Moreover, we did not observe the Cassie-Wenzel transition during the evaporation. Similarly, as shown in Fig. 4(e), on the hierarchical surface with a large L (mn40), we can clearly see that there exists a vapor layer between the droplet and substrate during the evaporation, inhibiting the complete Cassie-Wenzel transition.

The unique evaporation phenomenon on a hierarchical surface offers several advantages for biosensing. First, the

absence of a sticky CCL evaporation mode enabled by the presence of nanoscale roughness on hierarchical surfaces significantly decreases the solid-molecule interaction, leading to minimal molecule loss during the transport and enrichment process. Moreover, since the transduction structures for biosensing are usually located on the top of a surface, the formation of a composite state on the hierarchical surfaces at the late stage of evaporation might significantly promote the interaction between molecules diluted in the droplet and the transduction or sensing structures. Such a novel detection strategy eliminates the need for extra filtration steps, allowing for the detection of molecules at a very low concentration level.

In summary, we systematically investigated the full spectrum of contact line dynamics during the droplet evaporation based on microscopic and macroscopic observations and found that the contact line dynamics exhibited remarkable dependence on the geometric arrangement of the substrate. We developed general models to accurately predict the CCL-CCA transition onset time and critical base size at the Cassie-Wenzel transition. Interestingly, we demonstrated the significance of incorporating line tension in the analysis of energy states of droplets, especially when the evaporating droplet shrinks to a size comparable to the feature size of the solid roughness. We further show that the presence of nanoscale roughness on hierarchical surfaces not only prevents the onset of contact line pinning at the early stage of evaporation but also leads to the formation of a composite droplet without transiting to the sticky Wenzel state. The unique evaporation phenomena on hierarchical surfaces, coupled with the ability to control the contact line and wetting transition dynamics, might provide important insights for the design of robust superhydrophobic surfaces for various applications.

This work was supported by the Early Career Scheme Grant (No. 9041809), National Natural Science Foundation of China (No. 51276152) and National Program on Key Research Project (No. 2012CB933301), Centre for Functional Photonics at CityU, HKUST Direct Allocation Grant (No. DAG08/09.EG03), and RGC General Research Fund (621110). The authors also thank Professor Howard Stone for many useful discussions.

*Corresponding author.
zuanwang@cityu.edu.hk

[1] M. Nosonovsky and B. Bhushan, Nano Lett. **7**, 2633 (2007).
[2] K. -H. Chu, R. Xiao, and E. N. Wang, Nature Mater. **9**, 413 (2010).
[3] C. Duprat, S. Protère, A. Y. Beebe and H. A. Stone, Nature (London) **482**, 510 (2012).
[4] Y. Zheng, H. Bai, Z. Huang, X. Tian, F.-Q. Nie, Y. Zhao, J. Zhai, and L. Jiang, Nature (London) **463**, 640 (2010).
[5] R. Truesdell, A. Mammoli, P. Vorobieff, F. van Swol and C. J. Brinker, Phys. Rev. Lett. **97**, 044504 (2006).
[6] H. Liu, S. Szunerits, and W. Xu, ACS Appl. Mater. Interfaces **1**, 1150 (2009).
[7] N. A. Patankar, Langmuir **20**, 8209 (2004).
[8] X. Chen, J. Wu, R. Ma, M. Hua, N. Koratkar, S. Yao, and Z. Wang, Adv. Funct. Mater. **21**, 4617 (2011).
[9] J. B. Boreyko and C. H. Chen, Phys. Rev. Lett. **103**, 184501 (2009).
[10] F. De Angelis *et al.*, Nature Photon. **5**, 682 (2011).
[11] L. Gao and T. J. McCarthy, Langmuir **22**, 6234 (2006).
[12] W. Ren and W. E, Phys. Fluids **23**, 072103 (2011).
[13] M. Gross, F. Varnik, and D. Raabe, Europhys. Lett. **88**, 26 002 (2009).
[14] H. Gelderblom, Á G. Marín, H. Nair, A. van Houselt and L. Lefferts, Phys. Rev. E **83**, 026306 (2011).
[15] W. Xu and C. H. Choi, Phys. Rev. Lett. **109**, 024504 (2012).
[16] R. Bhardwaj, X. Fang, P. Somasundaran, and D. Attinger, Langmuir **26**, 7833 (2010).
[17] R. D. Deegan, O. Bakajin, T. F. Dupont, G. Huber, S. R. Nagel and T. A. Witten, Nature (London) **389**, 827 (1997).
[18] P. J. Yunker, T. Still, M. A. Lohr and A. G. Yodh, Nature (London) **476**, 308 (2011).
[19] P. Tsai, R. G. H. Lammertink, M. Wessling, and D. Lohse, Phys. Rev. Lett. **104**, 116102 (2010).
[20] K. R. Khedir, G. K. Kannarpady, H. Ishihara, J. Woo, S. Trigwell, C. Ryerson, and A. S. Biris, J. Phys. Chem. C **115**, 13 804 (2011).
[21] G. McHale, S. Aqil, N. J. Shirtcliffe, M. I. Newton and H. Y. Erbil, Langmuir **21**, 11 053 (2005).
[22] C. H. Choi and C. J. Kim, Nanotechnology **17**, 5326 (2006).
[23] V. Jokinen, L. Sainiemi, and S. Franssila, Adv. Mater. **20**, 3453 (2008).
[24] N. A. Malvadkar, M. J. Hancock, K. Sekeroglu, W. J. Dressick and M. C. Demire, Nature Mater. **9**, 1023 (2010).
[25] S. M. Rowan, M. I. Newton and G. McHale, J. Phys. Chem. **99**, 13 268 (1995).
[26] Y. S. Yu, Z. Wang, and Y. P. Zhao, J. Colloid Interface Sci. **365**, 254 (2012).
[27] D. R. Lide, *CRC Handbook of Chemistry and Physics* (CRC, Boca Raton, FL, 2009), 90th ed.
[28] H. Kusumaatmaja, M. L. Blow, A. Dupuis, and J. M. Yeomans, Europhys. Lett. **81**, 36 003 (2008).
[29] M. Reyssat, J. M. Yeomans and D. Quéré, Europhys. Lett. **81**, 26 006 (2008).
[30] S. Moulnet and D. Bartolo, Eur. Phys. J. E **24**, 251 (2007).
[31] P. Forsberg, F. Nikolajeff and M. Karlsson, Soft Matter **7**, 104 (2011).
[32] T. Liu, W. Sun, X. Sun, and H. Ai, Langmuir **26**, 14 835 (2010).
[33] W. Li and A. Amirfazli, Adv. Colloid Interface Sci. **132**, 51 (2007).
[34] K. Rykaczewski, W. A. Osborn, J. Chinn, M. L. Walker, J. H. J. Scott, W. Jones, C. Hao, S. Yao, and Z. Wang, Soft Matter **8**, 8786 (2012).
[35] J. W. Gibbs, *The Scientific Papers of J. Willard Gibbs* (Dover, New York, 1961), Vol. 1, p. 288.
[36] A. Amirfazli and A. W. Neumann, Adv. Colloid Interface Sci. **110**, 121 (2004).
[37] T. S. Wong and C. M. Ho, Langmuir **25**, 12 851 (2009).
[38] E. Bormashenko, J. Colloid Interface Sci. **360**, 317 (2011).

[39] C. A. Ward and J. Wu, Phys. Rev. Lett. **100**, 256103 (2008).
[40] E. R. Jerison, Y. Xu, L. A. Wilen and E. R. Dufresne, Phys. Rev. Lett. **106**, 186103 (2011).
[41] D. Hilbert and S. Cohn-Vossen, *Geometry and the Imagination* (Chelsea, New York, 1999), pp. 37–38.
[42] G. H. Hardy, *Ramanujan: Twelve Lectures on Subjects Suggested by His Life and Work* (Chelsea, New York, 1999), p. 67, 3rd ed.
[43] T. L. Lai, H Robbins and C. Z. Wei, Proc. Natl. Acad. Sci. U.S.A. **75**, 3034 (1978).
[44] M. Abramowitz and I. A. Stegun, *Handbook of Mathematical Functions* (Dover, New York, 1972).
[45] See Supplemental Material at http://link.aps.org/supplemental/10.1103/PhysRevLett.109.116101 for the calculation of the number of internal pillars (N_1) and external pillars (N_2), the liquid surface area contacting with the external pillars $A_{\mathrm{sl-ex}}$, and the total inside ($N_2 L_{ABC}$) and outside arc length ($N_2 L_{ADC}$) of water contacting with the external pillars.
[46] R. E. Johnson, Jr. and R. H. Dettre, Adv. Chem. Ser. **43**, 112 (1964).